A Novel Filter-Based Anomaly Detection Framework for Hyperspectral Imagery

WENZHENG WANG[ID]**[1], WEI SONG[2], ZHEN LI[3], BOYA ZHAO**[ID]**[3,4], AND BAOJUN ZHAO[5]**
[1]School of Electronics Engineering and Computer Science, Peking University, Beijing 100081, China
[2]School of New Media, Beijing Institution of Graphic Communication, Beijing 100086, China
[3]Aerospace Information Research Institute, Chinese Academy of Sciences, Beijing 100094, China
[4]Key Laboratory of Digital Earth Science, Chinese Academy of Sciences, Beijing 100094, China
[5]Beijing Key Laboratory of Embedded Real-Time Information Processing Technology, Beijing Institute of Technology, Beijing 100081, China

Corresponding author: Zhen Li (lizhen02@aircas.ac.cn)

ABSTRACT Hyperspectral images stand out from other remote sensing images in anomaly target detection because they contain unique distinguishing spectral information and attract great interest in applications of search and rescue. However, most of the popular techniques for hyperspectral anomaly detection tasks focus on improving accuracy with complicated algorithms and face difficulty in efficiently balancing performance and complexity. In this paper, we propose a novel anomaly detection approach using a selected band image extracted from the band selection model combined with an image filter. Singular value decomposition (SVD) is adopted for spectral dimensionality reduction. A dual-window guided filter is constructed to highlight the potential anomaly targets. To quickly calculate the abnormity degree, we design an efficient diagonal matrix operation to achieve the energy of each pixel, and a spatial regulation model is designed to enhance the subpixel target detection performance. Extensive experiments conducted on two real-world hyperspectral datasets demonstrate that, compared with the existing relevant state-of-the-art approaches, the proposed method requires less detection time and achieves higher detection accuracy.

INDEX TERMS Hyperspectral image analysis, remote sensing, anomaly detection, SVD, guided filter.

I. INTRODUCTION

Hyperspectral imaging (HSI) records hundreds of narrow contiguous bands that provide deterministic spectral information about different objects over the visible light spectrum to the near-infrared (NIR) spectrum [1], [2]. Therefore, HSIs can be considered 3-D cube data, which provides an intrinsic advantage for many real-world applications and has received broad and increasing attention for many years [3]–[6]. Hyperspectral image anomaly detection plays an important role in these applications and research. [7], [8].

In essence, anomaly detection can be regarded as unsupervised target detection that aims to extract the unusual spectral signature from the background. In contrast to supervised target detection, there is no prior knowledge of the target's spectral signature [9]. It is well known that the apriority target spectra selected from actual scenes are difficult and collected from the laboratory environment may be unusable in actual

scenes. Therefore, unsupervised anomaly detection is more useful and conforms to the tasks in real-world applications.

However, hyperspectral image anomaly detection usually suffers from two main issues: 1) the lower spatial resolution results in the distortion of the spectrum, which makes the detection performance unsatisfactory, and 2) the higher spectral resolution results in a larger data volume, which makes processing more difficult. Hence, anomaly target detection is an extremely challenging task.

Anomaly detection has been widely researched in recent decades. Based on the approach to estimate the abnormity degree of the potential anomaly target and the background, the current HSI anomaly detection method can be divided into two categories. One category uses the statistical analysis method to isolate the spectra that conform to the designed spectral distribution model. The other category usually uses the low-rank or sparse character of HSI to extract the anomaly target.

For the statistical-based anomaly detection method, the RX detector [10] assumes that the spectral signature in the HSI

The associate editor coordinating the review of this manuscript and approving it for publication was Qingli Li[ID].

follows a multivariate Gaussian distribution, and then, the distance between the spectrum under test and the spectrum within the local or global background in the whitened space is calculated to describe each spectrum's abnormity degree. Even the real-world spectrum signature rarely follows the designed Gaussian assumption; however, benefiting from the low computational complexity and fast process speed, the RX method is still widely used and is considered the benchmark method among most classical anomaly detection algorithms [11], [12]. Based on this, local RX measures the local areas surrounding the test pixel and can acquire better performance at the expense of computational cost [13]. The kernel-based RX method adopts kernel methods to project the background spectral information into a higher dimensional feature space, i.e., kernel RX [14] and cluster kernel RX [15].

For low-rank or sparse-based methods, the typical example is the low-rank and sparse representation (LRASR) anomaly detection method, which assumes that the HSI data are distributed in a multidimensional linear subspace and constructs a locally sparse constraint to overcome the influence of a complex background [16]. Other methods that fall into this category use different HSI backgrounds or data constraint models to extract the anomaly spectra. For example, anomaly detection tasks are regarded as a matrix decomposition problem with the minimum volume constraint for the multimodular background and sparsity constraint for the anomaly image pixels [17]. The RPCA method uses low-rank and sparse constraints to separate the HSI data into background and target matrices [18]. The LSMAD method utilizes RPCA and RXD to obtain the background model with low-rank characteristics [19]. Moreover, spectral unmixing and low-rank decomposition are combined to realize anomaly target detection [20].

Each of these algorithms improves a specific procedure in either obtaining a background description or considering sparsity and achieves better performance than classical methods. However, they dispose of HSI data by using spectral characteristics more than spatial characteristics, and the unique 3-D characteristics of HSI data are not fully used.

Benefiting from high flexibility, unmanned aerial vehicles (UAVs) have been widely used in real-world applications, i.e., search and track [21], and UAV platform-based hyperspectral remote sensing will be a trend. However, the aforementioned methods with complex calculations are not suitable for this platform with limited computing resources to realize high timeliness constraint tasks. Then, the detection performance and computational complexity should be equally considered. Unlike previous works, which usually focus on one of the two issues, our approach aims to solve both issues.

The main novelties of our work are presented in four aspects:

1) A new spatial-spectral combined framework is proposed, which can take both detection performance and computational complexity into account.

2) An effective dual-window guided filter method is developed to achieve a more accurate background description and significantly highlight the potential targets.

3) An effective matrix operation strategy is designed to quickly accumulate the abnormity degree of each pixel.

4) A spatial regulation model inspired by the point diffusion effect is established to enhance the subpixel anomaly target detection performance.

To address the two issues mentioned earlier, our method modified guided filter-based background description model to purify the background and highlight the potential anomaly targets. Moreover, a spatial regulation model is built to further improve the subpixel anomaly detection performance. For the second issue, SVD is exploited to remove the redundancy band images, and a more efficient difference calculation norm is designed to evaluate the abnormity degree of each pixel. In the proposed framework, we extend the traditional image processing method for hypercube hyperspectral images, and the abnormal target has been described from both spatial and spectral domains.

Using these novel techniques, the proposed framework is more suitable for hyperspectral image anomaly detection tasks with the following advantages. 1) Faster detection. Only selected band information is used for detection tasks and the complex iteration process is abandoned. 2) More reliable results. The dual-window guided filter structure achieves a much more robust background description for complex scenes.

The remainder of this paper is organized as follows. Section II explains the motivation of our framework. Section III overviews the proposed framework and expounds the method in detail, including SVD-based band selection, dual-window guided filtering, and contrast description calculations. Section IV demonstrates the simulation results comparing the proposed method and other relevant state-of-the-art hyperspectral anomaly target detection methods. Section V concludes the paper.

II. MOTIVATION

Anomalies are defined as observations that are different from their neighbouring background [22]. However, anomaly targets in hyperspectral images have unique characteristics; they not only show different spectral curve changes regularly with the background in the spectral domain but also present different values among the surrounding pixels in some single-band images in the spatial domain. Combined with the main issues mentioned before, we generally discuss the philosophy of our framework in the following.

A. SPATIAL-SPECTRAL COMBINED CHARACTER

HSI is a 3-D cube data, as shown in Fig. 1, which contains a more elaborate spectrum signature than traditional grey or colour images and leads to the unique characteristics of HSI. In this section, we employ the HSI characteristics to analyse the feasibility and rationality of the proposed method from both spatial and spectral dimensions.
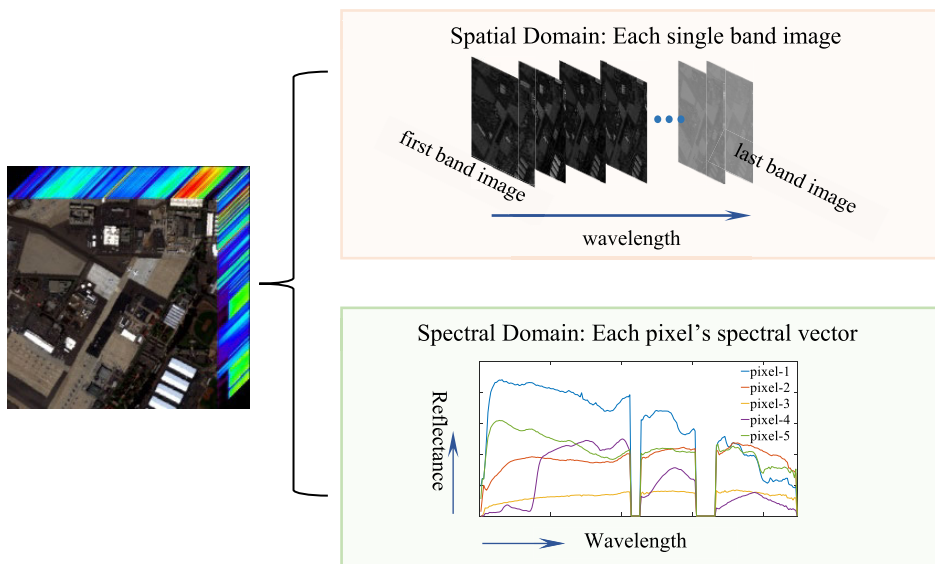
FIGURE 1. Hyperspectral image description in the spatial and spectral domains.

In Fig. 1, each HIS band can be seen as a single image of a certain band that has the same characteristics as a grey image. The main difference between them is the physical meanings of every pixel's value. For the single-band HSI image, the value represents the radiance or reflectance characteristics of this certain band for the observation region. For the grey image, the value represents the energy of the total visible light band and reflects the total variation in the wideband range. Then, we can employ the image processing method designed for the grey image to deal with this kind of single-band image.

Anomaly targets show different radiance or reflectance values compared with their neighbouring pixels in the single-band image. Then, in this paper, the anomaly detection procedure for signal band images is seen as a filtering process for finding unusual pixels. The more purely the background description we established, the more easily it is to separate anomaly targets.

Inspired by the digital image smoothing method that can remove abnormal points by replacing the centric pixels from its surrounding neighbours, we exploit one of these kinds of methods to deal with the signal band HSI image to achieve a pure background description. By comparing the background and original signal band images, we can obtain a map to describe the abnormal degree of each pixel in this certain band image.

B. SPECTRAL DIMENSIONALITY REDUCTION

HSI records the radiance or reflectance characteristics of the observation region and organizes this information by wavelength. Then, HSI can be seen as a data cube consisting of different pixels, and each pixel contains a one-dimensional spectrum vector. By comparing the value change or distribution variation in the spectrum vector, the abnormal spectrum vector can be extracted.
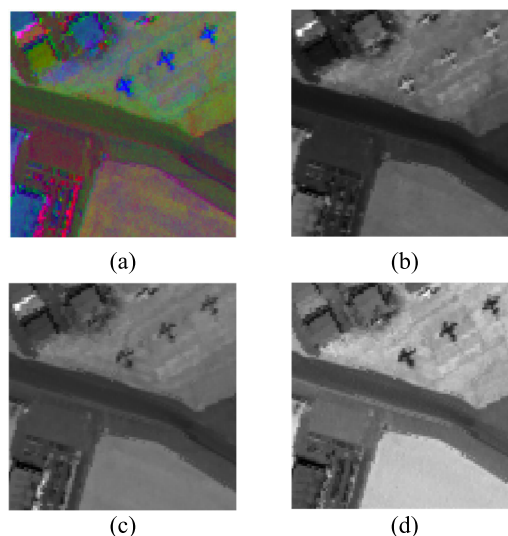

FIGURE 2. Visual comparison of difficult contrast band images in the AVIRIS dataset and SVD selected band images. (a) Pseudocolour image and (b)-(d) the 5th, 50th, and 180th band images.

However, too much spectral band not only provides abundant spectral information but also increases the hyperspectral image redundancy. As Fig. 2 shows, some band images are unsuitable for detecting anomalies due to their low contrast against the background.

Fig. 2 describes the hyperspectral image collected by the airborne visible infrared imaging spectrometer (AVIRIS) sensor. Fig. 2 (a) is the pseudocolour image of this region, and Fig. 2 (b)-(d) is the single-band image at the 5th, 50th and 180th bands. We can see that there are three airplanes in this scene, but different band images present different discrimination abilities to distinguish the targets. Fig. 2 (c) (the 50th band) presents lower contrast than that in Fig. 2 (b) and (d) (the 5th and 180th bands).
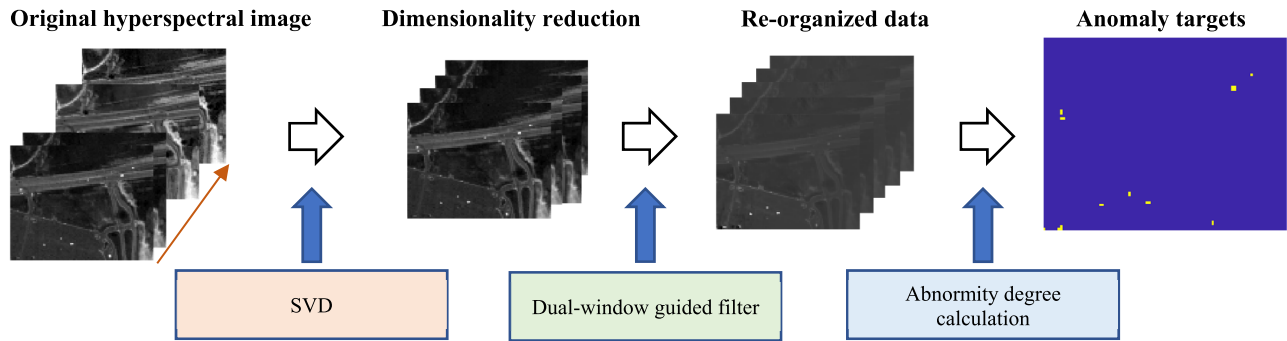
FIGURE 3. Proposed anomaly detection framework.

These low-contrast bands are counterproductive to target detection, and removing those redundancy bands needs to be applied. SVD is an effective tool for feature extraction and image decomposition and is also widely used for feature decomposition in dimension reduction tasks. Then, we exploit the SVD model into our framework to remove the redundant spectral band and select some bands that contain observation scene information for further analysis.

Moreover, hyperspectral images often contain noise, which can change the target spectral curves and influence the detection result. The SVD model also provides excellent anti-noise ability [23] since most of the random noise can be regarded as a high-frequency component in the images.

C. ROBUST BACKGROUND DESCRIPTION

Hyperspectral images are often collected by airplanes or satellite platforms, which contain a wide field of view and lead to observation areas consisting of many different ground surfaces. The complex features cause confusion between anomaly targets and similar edge areas, such as buildings or roads, which may also appear abnormal against the background.

Moreover, complex surfaces result in a complex spectral distribution situation and make it more difficult to build an effective background description model. Then, the complex surface severely restricted the detection performance of statistics-based methods.

To better detect the anomalies, we adopt the guided filter [24] to achieve the purified background description. By removing the background, the potential anomaly targets are highlighted in each single-band image. However, the original guided filter has a risk of removing the single-pixel or subpixel targets in the process of smoothness of the single-band image. In this paper, we design a dual-window structure to protect the single- and subpixel potential anomaly targets.

III. METHODS

In this paper, we propose a novel HSI anomaly detection framework depicted in Fig. 3. There are four modules in the framework: SVD-based band selection to reduce the spectral dimensionality, a dual-window guided filter to highlight the potential targets, matrix operations to achieve the abnormity

degree, and a spatial regularization model to obtain a better detection performance. The details of our proposed framework are explained in the rest of Section III.

A. SVD-BASED BAND SELECTION

As mentioned before, HSI contains a low-contrast abundant spectral band, and only a few high contrast bands are actually suitable for anomaly target detection tasks. We exploit the SVD model to select the band that contains the most content for further anomaly detection.

Assume that $I \in R(L \times M \times N)$ refers to a 3-D HSI image, where M, N and L are the width, height and bands, respectively. Then, the HIS data I can be reshaped into a 2-D matrix $X \in R^{(L \times (M \cdot N))}$, and it can be decomposed into matrices U, Σ and V^T. It is expressed as:

$$X = U \Sigma V^T \tag{1}$$

where U is an $L \times L$ orthogonal matrix with eigenvectors of XX^T in its columns, Σ is an $L \times (M \cdot N)$ matrix with the square root of eigenvalues of XX^T or X^TX as its diagonal elements, and V is a $(M \cdot N) \times (M \cdot N)$ orthogonal matrix with eigenvectors of X^TX in its columns. Since the SVD is efficient in capturing the directions (vectors) explaining most of the variability, a relatively small number of basis vectors tends to explain more than 99.99% of the overall variability [23], and it is expressed as:

$$X_{L \times (M \cdot N)} = U_{L \times L} \Sigma_{L \times (M \cdot N)} V^T_{(M \cdot N) \times (M \cdot N)}$$
$$\approx U_{L \times k} \Sigma_{k \times k} V^T_{k \times (M \cdot N)} \tag{2}$$

Then, we adopt the first k eigenvalues considered in SVD-based band selection., i.e., the first k most informative bands are selected, and the rest are discarded as redundancy bands.

B. DUAL-WINDOW GUIDED FILTER
1) ORIGINAL GUIDED FILTER
Anomaly targets, especially subpixel targets showing sparsity against the background, we exploit the guided filter to smooth the image and achieve a robust background description. The guided filter has shown satisfactory ability to preserve the large scale of edges and smooth background information [24], [25]. Assume that the guide image, filtering input
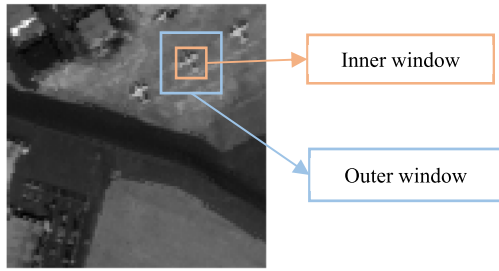
FIGURE 4. Dual-window guided filter structure.

FIGURE 5. Abnormity degree calculate.

image, and filtering output image are I_G, I_{IN} and I_{GF}, respectively. The guided filter is driven by a local linear model as follows:

$$I_{GF} = a_k I_G(i) + b_k, \quad \forall i \in \omega_k \quad (3)$$

where (a_k, b_k) are the linear coefficient parameters, i is the index of a pixel, and k is the index of a local window with a radius w. Assume I_{IN} is the filtering input image, and the minimized reconstruction error between I_{IN} and I_{GF} is defined as follows:

$$a_k = \frac{\frac{1}{|\omega|} \sum_{i \in w_k} I_G(i) I_{IN}(i) - \mu_k \bar{I}_{IN}(k)}{\sigma_k^2 + \varepsilon} \quad (4)$$

$$b_k = \bar{I}_{IN}(k) - a_k \mu_k \quad (5)$$

where μ_k and σ_k^2 are the mean and variance in I_G in window k, and ε is a regularization parameter controlling the degree of smoothness. The output of guider filtering is computed by:

$$
\begin{aligned}
I_{GF}(i) &= \frac{1}{|w|} \sum_{k:i \in w_k} (a_k I_i + b_k) \\
&= \bar{a}_i I_g(i) + \bar{b}_i
\end{aligned}
\quad (6)
$$

where $\bar{a}_i$ and $\bar{b}_i$ are the average of a and b, respectively, on the window k_i centre at i.

2) DUAL-WINDOW GUIDED FILTER STRUCTURE

As a guided filter is designed for grey images or colour images, it cannot be utilized for HSI cubes directly. Then, we use SVD to select some single-band images and extend the original guided filter into a dual-window structure (as shown in Fig. 4.) to improve the detection probability for anomaly targets.

For each single-band image, targets are influenced deeply by their nearest neighbour pixels but relatively shallower for further neighbour pixels. Then, if we let $Diff_i$ be the output of a single-band image, it can be described as:

$$Diff_i = Inner_i - Outer_i \quad (7)$$

where $Inner_i$ and $Outer_i$ represent the results of the guided filter by using inner and outer filtering windows, respectively.

For the background region, the inner window filter and outer window filter obtain almost the same background description, and the difference of this region will be close to zero. For the region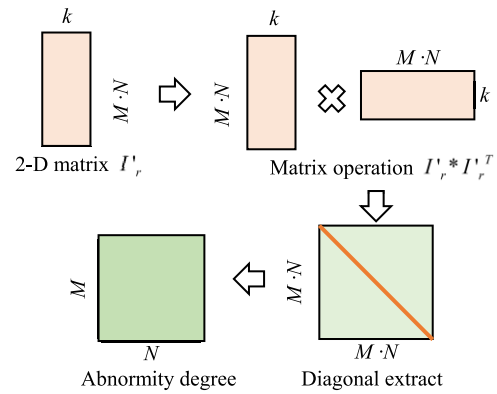 that contains anomaly targets, the outer window smooths the anomaly pixels with more background regions than the inner window. Then, the difference between these two windows will be greater than the situation without anomaly targets. The outer window builds the background description, but the inner window reserves the anomaly targets, and the difference between the inner and outer windows relatively enhances the anomaly targets.

C. ABNORMILTY DEGREE CALCULATION

For each selected single-band image, through the deviation calculation between the two windows mentioned above, we can obtain an enhanced different image in which the potential anomaly targets in the original single-band image can be highlighted.

We reorganize the different processed images into a new 3-D hypercube. Then, each pixel in the new data is reverted to a vector. However, differing from the original data, the background pixel vector is near zero, and the anomaly target vector is much larger than the zero vector in the hypercube. This phenomenon leads to different energies between the background and target vectors. Then, we use the energy to measure the abnormity degree of each pixel's vector from the reorganized data, and greater energy means a greater abnormity degree. To improve computational efficiency, we design a diagonal matrix operation to efficiently compute the energy of each pixel between the bands, as illustrated in Fig. 5. If we let d_i be the abnormity degree, for vector x_i, its energy can be described as:

$$d_i = x_i * x_i^T \quad (8)$$

The reorganized data I_r with the size $k \times M \times N$ is transformed into a 2-D matrix I_r' with the size $k \times (M \cdot N)$; then, the abnormity degree result D can be efficiently calculated as:

$$D = I'_r * I'^T_r \quad (9)$$

By using this approach, we can obtain a detection map in which the value equals each pixel's abnormity degree. This process is illustrated in Fig. 5.

D. SPATIAL REGULARIZATION MODEL

Mixed pixel and point spread phenomena widely exist in hyperspectral images of the real world. This leads to the target spectra being influenced by the background spectra around it and increases the missing alarm probability, especially for subpixel targets. To address this situation, inspired by the key technique in infrared target detection systems reported in [26], we design an efficient regularization model to enhance the abnormal subpixel spectral detection performance.

We modelled the mixed pixel and point spread phenomenon using the following formula:

$$I(x, y) = I_0 \exp \left\{ -\frac{1}{2} \left[\frac{(x - x_0)^2}{\sigma_x^2} + \frac{(y - y_0)^2}{\sigma_y^2} \right] \right\} \quad (10)$$

where I_0 is the anomaly detection result, (x_0, y_0) denotes the centre location of the candidate target, and σ_x and σ_y are the horizontal and vertical extent parameters, respectively. $I(x, y)$ represents the value of the surrounding location (x, y).

The subpixel target I_0 is surrounded by the direct neighbour domain and the diagonal neighbour domain, and they approximately contain the following relationships:

$$p = \frac{\ln I_0 - \ln M}{\ln I_0 - \ln N} \quad (11)$$

where I_M and I_N represent the average value of the direct and diagonal neighbour domains, respectively. p is the indicator to judge whether a subpixel target is a target and equals 0.5 only under ideal conditions. We set the protection interval of p to [0.3, 0.7]. For the subpixel target, we design a regulation function to enhance its abnormality degree as follows:

$$D_r = D_i \Bigg/ \left[\frac{1}{1 + \exp(-p)} \right] \quad (12)$$

where D_r is the enhanced abnormity degree of the subpixel target D_i. Thus, we can obtain a regulated detection result with more distinguishability.

IV. EXPERIMENTS AND DISCUSSION

Extensive experiments are conducted in this section. To evaluate the effectiveness and robustness of our method, we compare it with several outstanding hyperspectral anomaly detection methods (Global RX, Global Kernel-RX, Local RX, Local Kernel RX, robust PCA, LSMAD, LRASR, FrFE [27] and GTVLRR [28]) based on two real-world and public datasets.

We exploited receiver operating characteristic (ROC) curves to evaluate the performance of different algorithms [29]. ROC curves describe the varying relationship of P_D (probability of detection) changing with P_{FA} (false alarm) at different thresholds to measure the anomalies. P_D and P_{FA} are defined as follows:

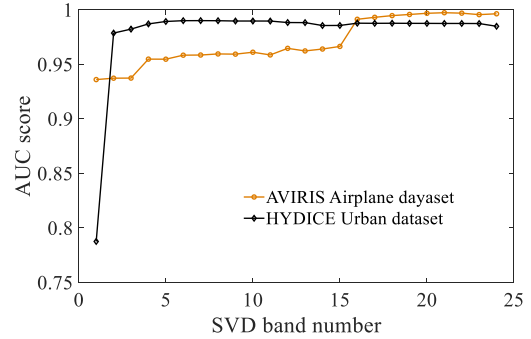$$P_D = \frac{N_{TT}}{N_T}, \quad P_{FA} = \frac{N_{FT}}{N_B} \quad (13)$$

FIGURE 6. AUC scores under different band numbers.

where N_{TT} is the number of correct detection target pixels and N_T is the total number of total true target pixels. N_{FT} represents the number of background pixels labelled as targets, and N_B indicates the total number of background pixels.

For a further comparison of the anomaly detector performance, another more frequently used performance measure named the area under the ROC curve (AUC) is applied to further evaluate the detection accuracy [30]. AUC calculates the area under the curve of ROC curves.

A. DATASETS

For a fair comparison, two widely used real-world hyperspectral anomaly detection datasets collected by different sensors and containing different surfaces are applied in the experiment.

1) HYDICE URBAN DATASET

The first scene is the most commonly used dataset in hyperspectral anomaly detection experiments; it was collected by the Hyperspectral Digital Imagery Collection Experiment (HYDICE) from a land cover region [31] and is composed of buildings, vegetation, roads, and vehicles. There are 21 sub- or pure pixels marked as anomalies in these data, whose size is 80 × 100, and the spatial resolution is 3 m. Moreover, the spectral bands of this dataset are 162 after removing 48 water absorption and low signal-to-noise bands.

2) AVIRIS AIRPORT DATASET

The second dataset is a part of an airport in San Diego collected by the Airborne Visible/Infrared Imaging Spectrometer (AVIRIS) [32]. In our experiment, the dataset consists of 100 × 100 pixels and 188 spectral channels after removing the bad bands with a 3.5 m spatial resolution. This dataset is composed of buildings, vegetation, runways, an apron, and three airplanes. As usual, those airplanes are marked as anomaly targets consisting of 64 pixels. However, we found that embedded roofs seem to be unusual spectra in this scene. Here, we still respect and follow the normal process and regard the three airplanes as anomalies.

B. PARAMETER ANALYSIS AND SETTING

1) THE NUMBER OF RESERVE BAND

In our framework, we exploit the SVD model to remove the redundancy band. Each band of SVD transformed data
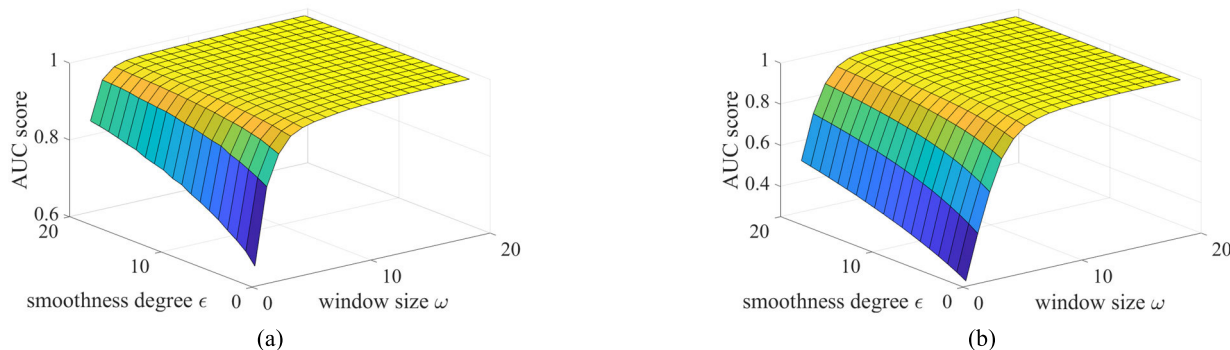
FIGURE 7. AUC scores under different filter parameters *w* and ε. Fig. 7 (a) and (b) show the AUC scores for the HYDICE Urban and AVIRIS Airport datasets, respectively.

describes different information components of the original hyperspectral image, and we need enough band information to establish the stable background description and highlight the potential targets. Then, we first test the proposed framework on two datasets with different reserve band numbers to find the best parameter setting.

As illustrated in Fig. 6, different datasets seem to need different reserve band numbers. For the HYDICE Urban dataset, a satisfactory AUC score was obtained under 5 reserve bands, and the detection performance remained stable when the band number increased. However, for the AVIRIS dataset, many more reserve bands were needed to obtain excellent detection performance. Then, for a fair comparison, we chose 20 SVD reserved bands in our experiment for further analysis.

2) FILTER PARAMETERS
The parameters of the designed dual-window guided filter include *w* and ε, which indicate the window size and degree of smoothness, respectively. In our dual-window structure, we set the outer window size twice over the inner window, and the outer window smoothness degree was ten times over the inner window. For simplicity to illustrate the performance of two parameters, we show the detection AUC score changes under two datasets with different outer filter parameters in Fig. 7.

In this parameter analysis experiment, we set *w* ranging from 2 to 20 and ε ranging from 2 to 20 to test the AUC scores. It seemed that the detection performance was sensitive to the window size *w*. For the HYDICE Urban dataset, better detection performance was obtained when *w* increased to 5. However, for the AVIRIS Airport dataset, satisfactory detection performance was obtained when *w* increased to 14. This situation is related to the size of anomaly targets, and the targets in the Airport dataset are much larger than the targets in the Urban dataset; thus, it may need a larger filter window size.

Although anomaly target detection is an unsupervised task, what we want to detect is guidance information to determine the filter window. In our experiment, we still followed stringent anomaly detection without any prior information, and

in the follow-up experiments, we set the same parameters $w = 15$ and $\varepsilon = 10$.

C. DETECTION PERFORMANCE ANALYSIS
In this section, we compare the proposed framework with several typical and newly proposed outstanding hyperspectral anomaly detection methods both qualitatively and quantitatively.

1) QUALITATIVE EVALUATION
For qualitative evaluation, we normalized the detection results to [0, 1] and binarized the result on the threshold values set according to the first 1% and 2% of the results of each algorithm. The results on the two datasets are illustrated in Fig. 8 and Fig. 9. For the HYDICE Urban dataset, Fig. 8 presents the acquired detection results of the compared methods. Fig. 8 (k) is the ground truth map, Fig. 8 (l) is the pseudocolour image, and (a) to (j) are the corresponding detection results of different methods. At threshold values set according to the first 1% value of the result under each method, FrFE and the proposed method correctly detect all the targets and remove most of the background. Other algorithms, i.e., Global RX, Global Kernel RX, and LRASR, have lost the targets within the red circle region marked in the ground truth map in Fig. 8 (k). This situation occurs because those targets contain a lower abnormity degree than many background regions, which interferes with the judgement of the anomaly targets.

For the AVIRIS Airport dataset, we set the threshold values according to the first 2% value of the result under each method. We can see that the shape of three airplanes was clearly visible in the detection results of LRASR, Global Kernel RX, FrFE and the proposed methods. The proposed method reserves complete target shapes, which means that there are discriminative differences between targets and the background and that the targets are more obvious and effortless for detection. Compared with other methods, the yellow block region and red block region marked in the pseudocolour image Fig. 9 (l) is the notable false detected region in many
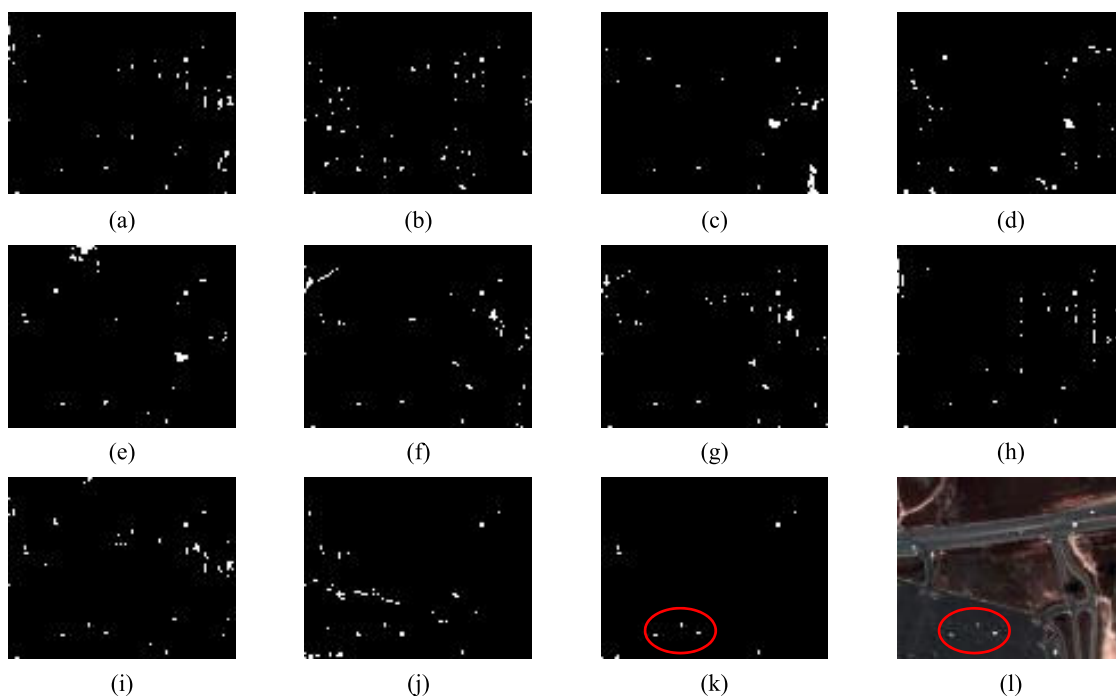
(a)　　　　　　　(b)　　　　　　　(c)　　　　　　　(d)

(e)　　　　　　　(f)　　　　　　　(g)　　　　　　　(h)

(i)　　　　　　　(j)　　　　　　　(k)　　　　　　　(l)

FIGURE 8. Detection results for the HYDICE Urban dataset: (a) Global RX, (b) Local RX, (c) Global Kernel RX, (d) Local Kernel RX, (e) LRASR, (f) RPCA, (g) LSMAD, (h) GTVLRR, (i) FrFE, (j) Proposed, (k) ground truth, (l) pseudocolour image.

(a)　　　　　　　(b)　　　　　　　(c)　　　　　　　(d)

(e)　　　　　　　(f)　　　　　　　(g)　　　　　　　(h)

(i)　　　　　　　(j)　　　　　　　(k)　　　　　　　(l)

FIGURE 9. Detection results for the AVIRIS Airport dataset: (a) Global RX, (b) Local RX, (c) Global Kernel RX, (d) Local Kernel RX, (e) LRASR, (f) RPCA, (g) LSMAD, (h) GTVLRR, (i) FrFE, (j) Proposed, (k) Ground Truth, (l) pseudocolour image.
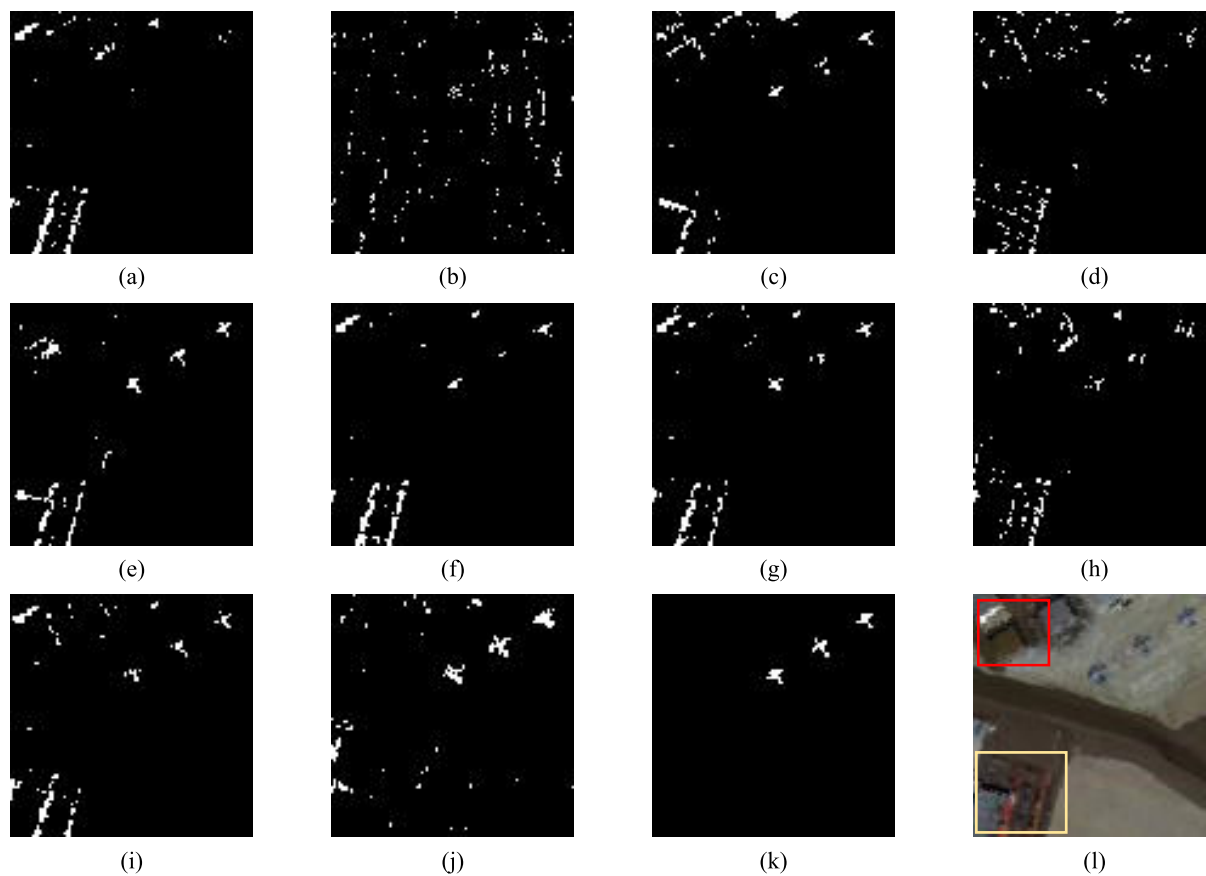
TABLE 1. AUC scores of the proposed framework and compared methods on two real-world datasets.

Dataset	HYDICE Urban dataset	AVIRIS Airport dataset
Golbal RX	0.9701	0.8862
Local RX	0.9825	0.8149
Global Kernel RX	0.9419	0.9793
Local kernel RX	0.9931	0.9688
LRASR	0.9554	0.9365
RPCA	0.9873	0.9761
LSMAD	0.9847	0.9748
GTVLRR	0.9641	0.9325
FrFE	0.9837	0.9795
Proposed	0.9977	0.9943

TABLE 2. The computational costs of different anomaly detection methods on the two datasets (in seconds).

Dataset	HYDICE Urban dataset	AVIRIS Airport dataset
Global RX	0.1824	0.1804
Local RX	23.1934	46.8122
Global Kernel RX	60.2382	106.1320
Local Kernel RX	492.3674	230.0724
LRASR	2.3818	2.8118
RPCA	28.8642	73.4604
LSMAD	7.7598	12.2942
GTVLRR	114.2318	134.391
FrFE	14.1748	20.848
Proposed	1.3302	1.8138

TABLE 3. The computation costs of each step (in seconds).

Dataset	HYDICE Urban dataset	AVIRIS Airport dataset
Dimensionality reduction	0.7292	1.1492
Dual-window guided filter	0.0666	0.078
Abnormity degree calculation	0.2172	0.3384
Spatial regulation	0.3172	0.2482

methods (i.e., LSMAD, RPCA), but those two regions are well restrained in our result.

2) QUANTITATIVE EVALUATION

The qualitative evaluation results on two datasets verified the effectiveness of the proposed anomaly detection framework. Considering that the visual assessments may be inaccurate, we employed the semi-log ROC curve to quantitatively evaluate the performance of all the methods, as shown in Fig. 10. Moreover, we repeatedly conducted the experiments 5 times, and the statistical average AUC scores are illustrated in Table 1.

Fig. 10 (a) shows the semi-log ROC curves of the first dataset. The probability of detection for our method grew much faster than that of the other methods and achieved the smallest false alarm rate when all the anomaly targets were detected.

For the second dataset, semi-log ROC curves are shown in Fig. 10 (b). We can see that the Global RX method achieved poor performance due to the complex background. The GTVLRR method showed better performance at low false alarm rates, but the fault-detected background region influenced (red block region marked in Fig. 9 (l)) the detection performance. For our methods, we still achieved the smallest false alarm rate when all the anomaly targets were detected.

As Table 1 shows, except for GTVLRR and LSMAD, the other methods all presented a stable performance, and the proposed method achieved the highest AUC score on both scenes, as expected. This demonstrates the effectiveness of the proposed hyperspectral anomaly detection framework.

D. TIME COST ANALYSIS

For a more comprehensive evaluation of the detection performance, we calculated the computational costs of different anomaly detection methods and present them in Table 2. Here, we repeated the Experiments 5 times to statistically calculate the average costs. The testing hardware and software conditions are listed as follows: Intel Core i7–4790 3.6 GHz CPU, 16 G DDR3 RAM, Windows 10, MATLAB R2020a.

In Table 2, we can see that our framework achieved faster detection speed than other state-of-the-art methods except for the Global RX model, which adopts linear projection to estimate the anomalies. Combining qualitative analysis, the results demonstrate that our method is an effective method for hyperspectral anomaly target detection tasks and shows outstanding performance compared with the state-of-the-art methods (i.e., LRASR, FrFE).

To comprehensively analyse the time costs of our methods, we calculated the computational costs of each processing step, and the results are listed in Table 3.

As illustrated in Table 3, the main computational costs were concentrated around the SVD-based spectral dimensionality reduction process (almost 60% of computational costs). A dual-window guided filter is efficient in highlighting potential anomalies, and abnormity degree calculation and spatial regulation also incur rare time costs. Then, a more concise dimensionality reduction method will further reduce the computational costs and improve the efficiency of the framework (i.e., PCA).

Based on the abovementioned analysis, our approach performs better in visualization results, detection accuracy, and time costs, and these results benefit from all aforementioned advantages: faster detection and more reliable results.

E. EACH STEP ANALYSIS

To demonstrate the importance of each step, we exploited the AUC score to evaluate the performance of the proposed framework under the situation without different steps. We reserve the abnormity degree calculation step as the basic
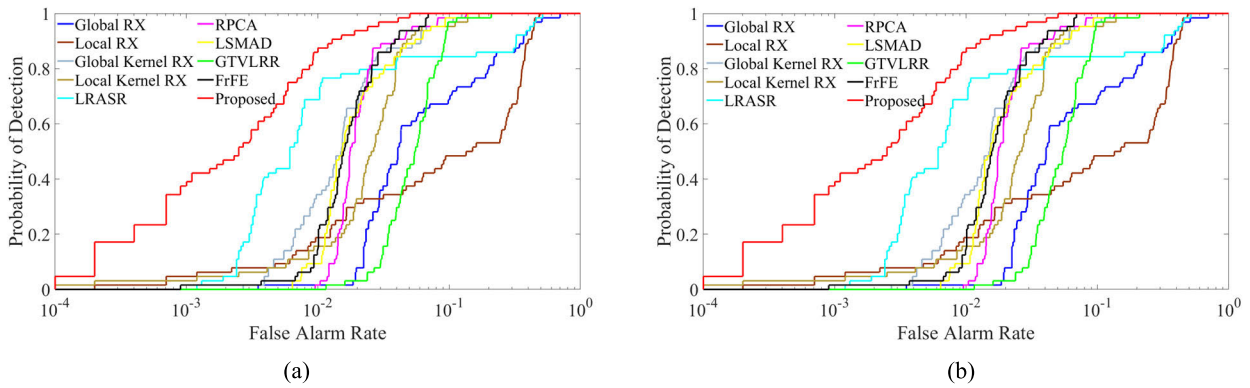
FIGURE 10. Semi-log ROC curves of anomaly detection methods on two datasets: (a) HYDICE Urban dataset, (b) AVIRIS Airport dataset.

TABLE 4. Auc score of the proposed method without different steps.

Steps	HYDICE Urban dataset
Only abnormity degree calculated	0.7566
Add SVD based dimension reduction	0.9801
Add Dual-window guided filter	0.9933
Add spatial regulation (Complete framework)	0.9977
Without SVD based dimension reduction	0.9904
Without dual-window guided filter	0.9743
Using basic guided filter	0.9902

process and gradually add other steps. Moreover, we test the situation when we without dimension reduction (dual-window guided filter, abnormity degree calculate and spatial regulation are reserved) or dual-window guided filter (dimension reduction, abnormity degree calculate and spatial regulation are reserved). Finally, we use the basic guided filter to replace the designed dual-window structure for further comparison.

As illustrated in Table 4, the detection performance is improved when we add each step until we obtain the complete framework that confirms the effectiveness of each step. When we removed the dimension reduction step or dual-window guided filter from the proposed framework, the AUC score was significantly reduced, which demonstrates the importance of the dimension reduction and dual-window guided filter. The result of adding the dual-window guided filter also means the framework without the spatial regulation model, compare with the result of the complete framework, we know that spatial regulation also improved the detection performance to some degree. There is an obvious contrast between using the dual-window guided filter and the basic guided filter, which demonstrates the effectiveness of the designed dual-window guided filter.

V. CONCLUSION

In this paper, we proposed a novel hyperspectral anomaly target detection framework based on spectral dimensionality reduction and a guided filter. In our framework, we exploited

SVD to reduce the spectral band. Then, we improved the guided filter into a dual-window structure to achieve a more purified background description and highlight the potential anomaly targets. After the filtering process, we reorganized the filtering results into a new 3-D hypercube and exploited an efficient matrix operation to achieve the abnormity degree of every pixel. Finally, we designed a spatial regulation model to enhance the detection performance, especially the sub-pixel anomaly targets. Extensive experiments demonstrate that our proposed framework outperforms the state-of-the-art methods in terms of both accuracy and computational costs. For future work, we will focus on a high-efficiency band selection and spectral dimensionality reduction strategy to further improve the performance of the proposed framework.

REFERENCES

[1] J. A. Richards, *Remote Sensing Digital Image Analysis: An Introduction*, 4th ed. New York, NY, USA: Springer, 2006.

[2] F. M. Lacar, M. M. Lewis, and I. T. Grierson, "Use of hyperspectral imagery for mapping grape varieties in the Barossa Valley, South Australia," in *Proc. Scanning Present Resolving Future, IEEE Int. Geosci. Remote Sens. Symp. (IGARSS)*, Sydney, NSW, Australia, Jul. 2001, pp. 2875–2877.

[3] F. van der Meer, "Analysis of spectral absorption features in hyperspectral imagery," *Int. J. Appl. Earth Observ. Geoinf.*, vol. 5, no. 1, pp. 55–68, Feb. 2004.

[4] T. J. Malthus and P. J. Mumby, "Remote sensing of the coastal zone: An overview and priorities for future research," *Int. J. Remote Sens.*, vol. 24, pp. 2805–2815, Nov. 2003.

[5] P. W. Yuen and M. Richardson, "An introduction to hyperspectral imaging and its application for security, surveillance and target acquisition," *Imag. Sci. J.*, vol. 58, no. 5, pp. 241–253, Oct. 2010.

[6] Z. Li, B. Zhao, and W. Wang, "An efficient spectral feature extraction framework for hyperspectral images," *Remote Sens*, vol. 12, no. 23, pp. 3967–3987, Dec. 2020.

[7] J. M. Bioucas-Dias, A. Plaza, G. Camps-Valls, P. Scheunders, N. M. Nasrabadi, and J. Chanussot, "Hyperspectral remote sensing data analysis and future challenges," *IEEE Geosci. Remote Sens. Mag.*, vol. 1, no. 2, pp. 6–36, Jun. 2013.

[8] W. Wang, B. Zhao, F. Feng, J. Nan, and C. Li, "Hierarchical sub-pixel anomaly detection framework for hyperspectral imagery," *Sensors*, vol. 18, no. 11, pp. 3662–3682, Oct. 2018.

[9] S. Matteoli, M. Diani, and G. Corsini, "A tutorial overview of anomaly detection in hyperspectral images," *IEEE Aerosp. Electron. Syst. Mag.*, vol. 25, no. 7, pp. 5–28, Jul. 2010.

[10] I. S. Reed and X. Yu, "Adaptive multiple-band CFAR detection of an optical pattern with unknown spectral distribution," *IEEE Trans. Acoust., Speech Signal Process.*, vol. 38, no. 10, pp. 1760–1770, Oct. 1990.

[11] N. M. Nasrabadi, "Regularization for spectral matched filter and RX anomaly detector," *Proc. SPIE*, vol. 6966, pp. 696604-1–696604-12, Apr. 2008.

[12] D. Borghys, V. Achard, S. R. Rotman, N. Gorelik, C. Perneel, and E. Schweicher, "Hyperspectral anomaly detection: A comparative evaluation of methods," in *Proc. 28th URSI Gen. Assem. Sci. Symp.*, İstanbul, Turkey, Aug. 2011, pp. 1–4.

[13] H. Kwon and N. M. Nasrabadi, "Kernel RX-algorithm: A nonlinear anomaly detector for hyperspectral imagery," *IEEE Trans. Geosci. Remote Sens.*, vol. 43, no. 2, pp. 388–397, Feb. 2005.

[14] C. Zhao, W. Deng, Y. Yan, and X. Yao, "Progressive line processing of kernel RX anomaly detection algorithm for hyperspectral imagery," *Sensors*, vol. 17, no. 8, pp. 1815–1831, Aug. 2017.

[15] J. Zhou, C. Kwan, B. Ayhan, and M. T. Eismann, "A novel cluster kernel RX algorithm for anomaly and change detection using hyperspectral images," *IEEE Trans. Geosci. Remote Sens.*, vol. 54, no. 11, pp. 6497–6504, Nov. 2016.

[16] Y. Xu, Z. Wu, J. Li, A. Plaza, and Z. Wei, "Anomaly detection in hyperspectral images based on low-rank and sparse representation," *IEEE Trans. Geosci. Remote Sens.*, vol. 54, no. 4, pp. 1990–2000, Apr. 2016.

[17] W. Wang, S. Li, H. Qi, B. Ayhan, C. Kwan, and S. Vance, "Identify anomaly component by sparsity and low rank," in *Proc. 7th Workshop Hyperspectral Image Signal Process., Evol. Remote Sens. (WHISPERS)*, 2015, pp. 1–4.

[18] J. Wright, A. Ganesh, S. Rao, and Y. Ma, "Robust principal component analysis: Exact recovery of corrupted low-rank matrices via convex optimization," in *Proc. Neural Inf. Process. Syst. (NIPS)*, Dec. 2009, pp. 289–298.

[19] Y. Zhang, B. Du, L. Zhang, and S. Wang, "A low-rank and sparse matrix decomposition-based Mahalanobis distance method for hyperspectral anomaly detection," *IEEE Trans. Geosci. Remote Sens.*, vol. 54, no. 3, pp. 1376–1389, Mar. 2016.

[20] Y. Qu, R. Guo, W. Wang, H. Qi, B. Ayhan, C. Kwan, and S. Vance, "Anomaly detection in hyperspectral images through spectral unmixing and low rank decomposition," in *Proc. IEEE Int. Geosci. Remote Sens. Symp. (IGARSS)*, Jul. 2016, pp. 1855–1858.

[21] C. Deng, S. He, Y. Han, and B. Zhao, "Learning dynamic spatial-temporal regularization for UAV object tracking," *IEEE Signal Process. Lett.*, vol. 28, pp. 1230–1234, 2021.

[22] C. Zhao, X. Wang, and G. Zhao, "Detection of hyperspectral anomalies using density estimation and collaborative representation," *Remote Sens. Lett.*, vol. 8, no. 11, pp. 1025–1033, Nov. 2017.

[23] P. Bajorski, E. J. Ientilucci, and J. R. Schott, "Comparison of basis-vector selection methods for target and background subspaces as applied to subpixel target detection," *Proc. SPIE*, vol. 5425, pp. 97–108, Aug. 2004.

[24] K. He, J. Sun, and X. Tang, "Guided image filtering," *IEEE Trans. Pattern Anal. Mach. Intell.*, vol. 35, no. 6, pp. 1397–1409, Jun. 2013.

[25] R. Karumuri and S. A. Kumari, "Weighted guided image filtering for image enhancement," in *Proc. 2nd Int. Conf. Commun. Electron. Syst. (ICCES)*, Coimbatore, India, Oct. 2017, pp. 545–548.

[26] X. Yan, J.-X. Peng, M.-Y. Ding, and D.-H. Xue, "An extended track-before-detect algorithm for infrared target detection," *IEEE Trans. Aerosp. Electron. Syst.*, vol. 33, no. 3, pp. 1087–1092, Jul. 1997.

[27] R. Tao, X. Zhao, W. Li, H.-C. Li, and Q. Du, "Hyperspectral anomaly detection by fractional Fourier entropy," *IEEE J. Sel. Topics Appl. Earth Observ. Remote Sens.*, vol. 12, no. 12, pp. 4920–4929, Dec. 2019.

[28] T. Cheng and B. Wang, "Graph and total variation regularized low-rank representation for hyperspectral anomaly detection," *IEEE Trans. Geosci. Remote Sens.*, vol. 58, no. 1, pp. 391–406, Jan. 2020.

[29] C.-I. Chang, "Multiparameter receiver operating characteristic analysis for signal detection and classification," *IEEE Sensors J.*, vol. 10, no. 3, pp. 423–442, Mar. 2010.

[30] N. Barakat and A. P. Bradley, "Rule extraction from support vector machines: Measuring the explanation capability using the area under the ROC curve," in *Proc. 18th Int. Conf. Pattern Recognit. (ICPR)*, Hong Kong, 2006, pp. 812–815.

[31] P. A. Mitchell, "Hyperspectral digital imagery collection experiment: Hydice," *Proc. SPIE*, vol. 2587, pp. 70–95, Nov. 1995.

[32] F. A. Kruse, A. B. Lefkoff, J. W. Boardman, K. B. Heidebrecht, A. T. Shapiro, P. J. Barloon, and A. F. H. Goetz, "The spectral image processing system (SIPS)—Interactive visualization and analysis of imaging spectrometer data," *Remote Sens. Environ*, vol. 44, pp. 145–163, May 1993.
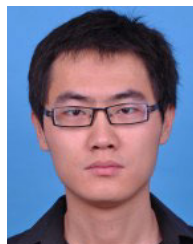
WENZHENG WANG received the Ph.D. degree from the School of Electrical and Information Engineering, Beijing Institute of Technology, Beijing, China, in 2019. He is currently a Post-doctoral Research Fellow with the School of Electronics Engineering and Computer Science, Peking University. His current research interests include hyperspectral/optical imagery target detection, feature selection, and machine learning.

WEI SONG received the Ph.D. degree in electronic science and technology from Beijing Institute of Technology (BIT), Beijing, China, in 2020. Since 2020, he has been engaged in teaching and research work at Beijing Institute of Graphic Communication (BIGC). His main research interests include digital media technology and machine learning.

ZHEN LI received the Ph.D. degree in information and communication engineering from Beijing Institute of Technology, Beijing, China, in 2021. He is currently an Assistant Professor with the Aerospace Information Research Institute, Chinese Academy of Sciences. His current research interests include computer vision, machine learning especially for hyperspectral images processing, image quality assessment, and its applications.

BOYA ZHAO was born in 1990. He received the Ph.D. degree from the School of Electrical and Information Engineering, Beijing Institute of Technology, Beijing, China, in 2019. He is currently an Assistant Professor with the Key Laboratory of Digital Earth Science, Aerospace Information Research Institute, Chinese Academy of Sciences, Beijing. His research interests include object detection in the complex background and on-board real-time information processing.

BAOJUN ZHAO received the Ph.D. degree in electromagnetic measurement technology and equipment from Harbin Institute of Technology (HIT), Harbin, China, in 1996. From 1996 to 1998, he was a Postdoctoral Fellow with Beijing Institute of Technology (BIT), Beijing, China. Since 1998, he has been engaged in teaching and research work at the Radar Research Laboratory, BIT. He has authored or coauthored over 100 publications. His main research interests include image/video coding and image recognition.

• • •